### Title

Facet-dependent photovoltaic efficiency variations in single grains of hybrid halide perovskite




### Journal

Nature Energy, 1(8)

### ISSN

2058-7546



### Authors

Leblebici, Sibel Y
Leppert, Linn
Li, Yanbo
et al.



### Publication Date

2016

### DOI

10.1038/nenergy.2016.93

Peer reviewed

nature energy

ARTICLES

PUBLISHED: 4 JULY 2016 | ARTICLE NUMBER: 16093 | DOI: 10.1038/NENERGY.2016.93

# Facet-dependent photovoltaic efficiency variations in single grains of hybrid halide perovskite

Sibel Y. Leblebici[1,2], Linn Leppert[1,3], Yanbo Li[4], Sebastian E. Reyes-Lillo[1,3], Sebastian Wickenburg[1], Ed Wong[1], Jiye Lee[1], Mauro Melli[1], Dominik Ziegler[1,5], Daniel K. Angell[1], D. Frank Ogletree[1], Paul D. Ashby[1], Francesca M. Toma[4], Jeffrey B. Neaton[1,3,6], Ian D. Sharp[4]* and Alexander Weber-Bargioni[1]*

**Photovoltaic devices based on hybrid perovskite materials have exceeded 22% efficiency due to high charge-carrier mobilities and lifetimes. Properties such as photocurrent generation and open-circuit voltage are influenced by the microscopic structure and orientation of the perovskite crystals, but are difficult to quantify on the intra-grain length scale and are often treated as homogeneous within the active layer. Here, we map the local short-circuit photocurrent, open-circuit photovoltage, and dark drift current in state-of-the-art methylammonium lead iodide solar cells using photoconductive atomic force microscopy. We find, within individual grains, spatially correlated heterogeneity in short-circuit current and open-circuit voltage up to 0.6 V. These variations are related to different crystal facets and have a direct impact on the macroscopic power conversion efficiency. We attribute this heterogeneity to a facet-dependent density of trap states. These results imply that controlling crystal grain and facet orientation will enable a systematic optimization of polycrystalline and single-crystal devices for photovoltaic and lighting applications.**

Hybrid organic–inorganic halide perovskites are a fascinating and highly promising class of materials for optoelectronic applications, since they are straightforward to fabricate[1–3] and have tunable direct bandgaps[4–6]. After only a few years of active research, polycrystalline thin-film perovskite photovoltaic (PV) devices[7–9] have reached power conversion efficiencies (PCEs) exceeding 22% (ref. 10) and have potential applications as light-emitting diodes (LEDs)[8,11], laser gain media[12], and photodetectors[13]. For PV devices, the rapid increase in PCE is astounding, considering that the origins of the highly efficient photovoltaic effect, as well as efficiency loss mechanisms, are not fully understood. Systematic optimization of efficiency requires understanding these fundamental processes at their native length scales.

Previous work on the macroscopic optoelectronic mechanisms revealed high charge-carrier mobilities[14–16] and long lifetimes[17], suggesting homogeneous performance within the active layer[18]. At the nanoscale, studies of charge separation processes concluded that devices are analogous to p–i–n junctions[19,20], and another study reported enhanced photocurrent along grain boundaries[21]. Recent studies found surprisingly strong inter-grain photoluminescence (PL)[22] and cathodoluminescence[23] heterogeneity, which suggests that optoelectronic properties, such as open-circuit voltage ($V_{OC}$), may also exhibit strong local variations[24]. These results highlight the pressing need to study local PV characteristics, such as $V_{OC}$ and short-circuit current ($I_{SC}$), to understand the factors affecting efficiency in these systems. However, while inorganic and polymer PV materials have been studied on the nanoscale using scanning probe techniques[25–27], no studies have yet determined the governing optoelectronic properties for perovskite PV devices at their native length scales (10–100 nm) or what limits their efficiency.

Here, we locally probe and map the parameters that determine PV device performance—$V_{OC}$, $I_{SC}$, and dark drift current ($I_D$)—close to their native length scales. This was accomplished by employing a customized conductive atomic force microscopy (cAFM) technique to provide insight into these critical PV performance-determining parameters with nm-scale resolution. Density functional theory (DFT) calculations on perovskite electronic structure were carried out to support the interpretation of experimental data. We find significant intra-grain heterogeneities, which arise from facet-dependent variations of surface defect states that strongly impact device-level PCE. As a result, the macroscopic PV and LED performance of lead halide perovskites could be optimized by controlling the crystal orientation and facets at interfaces for both polycrystalline and single-crystal devices[16].

## Photocurrent microscopy to probe local efficiency

We used two sets of methylammonium lead iodide chloride ($MAPbI_{3-x}Cl_x$) thin films, which were processed in parallel. One set was used to fabricate planar solar cells by depositing a hole transport layer (HTL, spiro-OMeTAD) and a gold top contact, resulting in an

[1]The Molecular Foundry, Lawrence Berkeley National Laboratory, Berkeley, California 94720, USA. [2]Department of Materials Science and Engineering, University of California, Berkeley, California 94720, USA. [3]Department of Physics, University of California, Berkeley, California 94720, USA. [4]Joint Center for Artificial Photosynthesis and Chemical Science Division, Lawrence Berkeley National Laboratory, 1 Cyclotron Road, Berkeley, California 94720, USA. [5]Scuba Probe Technologies LLC, 255 Lina Ave, Alameda, California 94501, USA. [6]Kavli Energy NanoSciences Institute at Berkeley, Berkeley, California 94720, USA. *e-mail: idsharp@lbl.gov; afweber-bargioni@lbl.gov

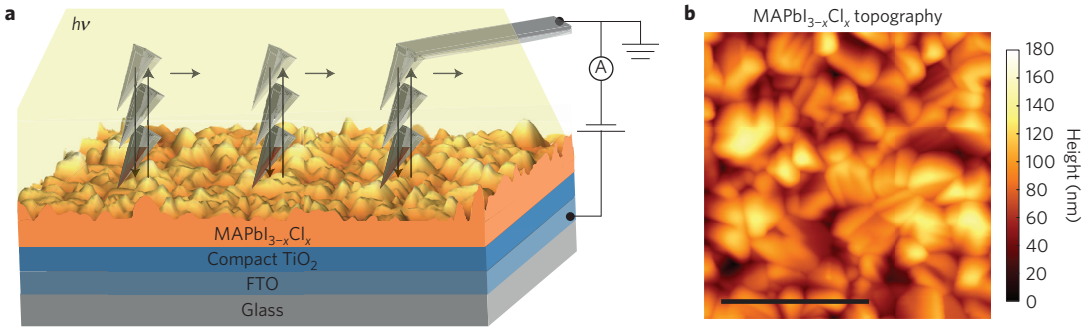


**Figure 1 | cAFM experiment on the surface of a $MAPbI_{3-x}Cl_x$ solar cell. a**, The entire sample surface is illuminated while a conductive AFM tip measures the photocurrent. Bias is applied to the fluorine-doped tin oxide (FTO) electrode and current is collected through the platinum-coated AFM tip at virtual ground. The arrows describe the approach–retract scan mode in which the tip approaches, measures, and retracts at each pixel, thereby minimizing potentially damaging tip–sample interactions. **b**, A representative topography image of a $MAPbI_{3-x}Cl_x$ thin film illustrates the large surface roughness. The scale bar is 1 μm.

average PCE of 15.7% (Supplementary Fig. 1). The second set was used as a half-cell for scanning probe analysis, omitting the HTL and top electrode to directly access the bare $MAPbI_{3-x}Cl_x$ surface. The large surface roughness of the perovskite material, together with strong tip–sample interactions, pose significant challenges for reproducible cAFM using contact mode scanning (Supplementary Fig. 2). Hence, we employed a modified cAFM technique in which, at each pixel, the tip approaches the surface, measures the photocurrent, retracts from the surface and moves to the next pixel, as shown in Fig. 1a. In contrast to conventional cAFM, this technique eliminates friction, which reduces tip–sample deterioration and material transfer, and maintains a constant contact area while measuring current. Figure 1b shows a representative topography measurement of the $MAPbI_{3-x}Cl_x$ surface; the average surface roughness is 19.1 nm and grain size is 142 ± 38 nm.

$I_{SC}$, $V_{OC}$ and $I_D$ were measured in this order on $MAPbI_{3-x}Cl_x$ solar cells under appropriate illumination and bias conditions: $I_{SC}$ under illumination at 0 V; $V_{OC}$ relative to a reference bias under illumination at forward reference biases between 0.1 and 0.7 V; and $I_D$ in the dark at 2 and 3 V forward bias. The $V_{OC}$ is segmented relative to an applied reference bias. That is, when the photocurrent measured by cAFM is negative, positive, or approximately zero, the $V_{OC}$ is less than, greater than, or approximately equal to the applied reference bias. This method of characterizing $V_{OC}$ was chosen because alternative techniques, such as collecting local current–voltage curves or scanning potentiometry maps, do not provide reproducible results on hybrid halide perovskites (see Supplementary Note 1). It is important to note that the conditions used to map $I_{SC}$ and $V_{OC}$ mitigate ion migration[28] because the tip is in contact with the sample for less than 2 ms, while electrical current from analogous macroscale devices is stable for at least hundreds of seconds (see Supplementary Note 2 and Supplementary Figs 4 and 5). Furthermore, we note that the maximum internal electric field is actually given by the built-in field at zero bias and is reduced as the tip bias approaches $V_{OC}$.

The topography image in Fig. 2a displays individual crystal grains and various crystal facets within these grains. The range of different grain shapes observed in the topography image is due to the lack of preferential grain orientation in these $MAPbI_{3-x}Cl_x$ films, as we have shown in a previous study using X-ray diffraction[3]. These measurements are reproducible (Supplementary Fig. 6) and free of artefacts from topography and tip–sample interactions, as we illustrate in detail in Supplementary Note 3.

Surprisingly, $I_{SC}$ and $V_{OC}$ (Fig. 2b,c) show not only strong local inter-grain but also intra-grain heterogeneity, which appear to be associated with the facets of individual grains. The photocurrent varies by up to an order of magnitude within individual grains ($I_{SC}$ map Fig. 2b). Importantly, we find that the average $I_{SC}$ for individual grains does not depend on grain size (Supplementary Fig. 7). This result contrasts with that of Nie *et al.*[29] and suggests that grain-size-dependent $I_{SC}$ may be different for the regime studied here, in which the grain size is smaller than the ~1 μm carrier diffusion length[14]. To ensure that the measured heterogeneity is not due to tip–sample interaction artefacts, we verified that $I_{SC}$ was not correlated with crystal height, different regions of constant topographic slope, or lateral and adhesion forces (Supplementary Fig. 8).

The $V_{OC}$ map shown in Fig. 2c also reveals intra-grain heterogeneity. This segmented map was obtained by measuring current at a forward reference bias of 0.6 V, which is near the macroscale $V_{OC}$ (0.51 V) obtained on a device with a Pt top contact in place of the HTL/Au to mimic the Pt cAFM tip–sample contact. As a result, all $V_{OC}$ values in the map are reported relative to the applied 0.6 V reference bias, as described above. As in the case of $I_{SC}$, the observed variation of $V_{OC}$ is most pronounced within individual grains, rather than between different grains.

As a metric for local PV performance, we define the efficiency indicator, which is assigned as 'high' in regions having a combination of high $V_{OC}$ and $I_{SC}$ and 'low' in regions of low $V_{OC}$ and $I_{SC}$. Note that, contrary to PCE, this efficiency indicator does not contain the fill factor. We could not make quantitative PCE maps, since this would require current–voltage curves at each pixel, for the experimental reasons described above. The efficiency indicator map in Fig. 2d was generated by overlaying topography, in grey scale, with pixels representing high efficiency in blue ($V_{OC} > 0.6$ V and $I_{SC} > 12$ pA) and low efficiency in red ($V_{OC} \leq 0.6$ V and $I_{SC} < 5$ pA). Considerable intra-grain heterogeneity can be seen. To exclude tip–substrate effects as a cause for the heterogeneity, we repeated $I_{SC}$ and $V_{OC}$ scans over the same region and observed no change in the heterogeneity; used tips of different materials and observed similar heterogeneity (Supplementary Fig. 9); and performed cAFM experiments on samples following deposition of a thin HTL layer of spiro-OMeTAD on the $MAPbI_{3-x}Cl_x$ (Supplementary Fig. 10) and observed again similar heterogeneity in $I_{SC}$. These tests clearly indicate that the observed spatial variation is an inherent feature of these PV devices and not an artefact of interactions between the tip and the sample material.

## Grain facet-dependent heterogeneity

The observed intra-grain heterogeneity in $I_{SC}$, $V_{OC}$ and efficiency indicator maps appear to be facet dependent when compared to the topography map. To test this observation statistically, the variance of $I_{SC}$ within facets was determined and compared to the $I_{SC}$ variance of facet-sized areas that were randomly placed over the $I_{SC}$ map. The facets were identified by calculating the

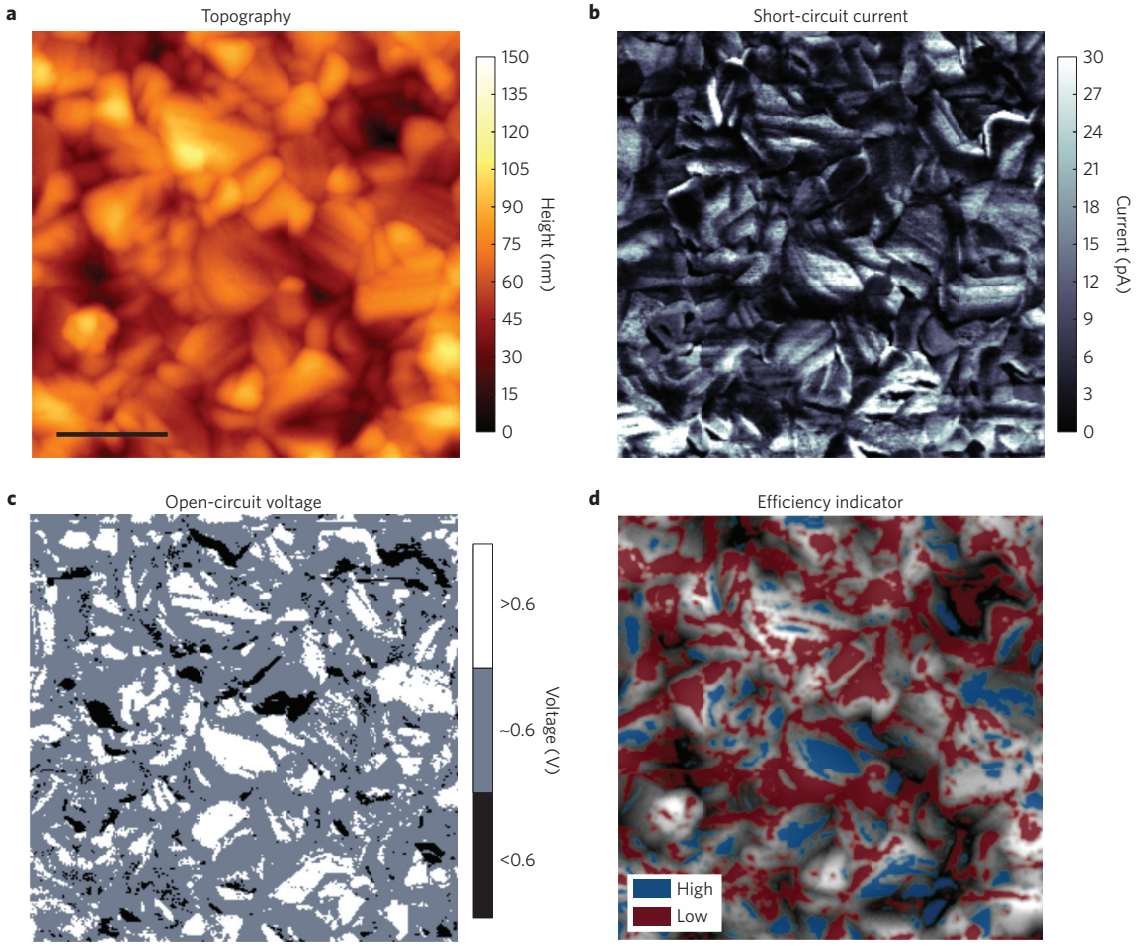


**Figure 2 | Intra-grain heterogeneity of $I_{SC}$, $V_{OC}$, and efficiency indicator. a**, Topography image corresponding to all current maps. Individual crystal grains and their facets are clearly visible. The scale bar is 500 nm. **b**, $I_{SC}$ map measured at 0 V bias under illumination. Similar $I_{SC}$ maps were measured on samples that included a thin HTL layer of spiro-OMeTAD on the $MAPbI_{3-x}Cl_x$ (Supplementary Fig. 10). **c**, Segmented $V_{OC}$ map measured under illumination relative to a forward reference bias of 0.6 V. Grey areas have $V_{OC}$ close to the reference bias, white areas above and black areas below. **d**, To compare heterogeneity of $I_{SC}$ and $V_{OC}$ to facets, areas in blue (high $V_{OC}$ and $I_{SC}$) and areas in red (low $V_{OC}$ and $I_{SC}$) are overlaid on the local topography, indicating that many grains have a specific crystal facet that provides higher performance. For enlarged images with marked grains see Supplementary Fig. 19.

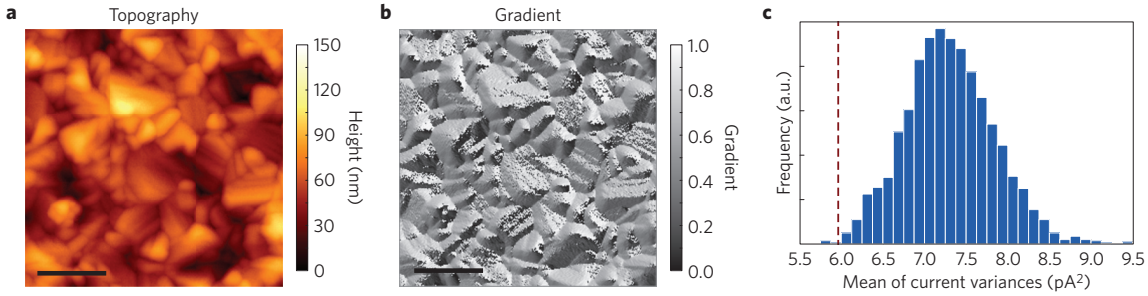


**Figure 3 | Facet-dependent $I_{SC}$ heterogeneity. a**, Topography image in same area as Fig. 2a. Grains are easily distinguished, but facets are more difficult to identify. Scale bar is 1 μm. **b**, Azimuthal gradient image calculated from the topography image. Facets (areas of constant slope) are clearly identified in the gradient image. **c**, Histogram of the mean of the $I_{SC}$ variances calculated for 2,000 sets of randomly placed squares that mimic the size and number of the identified facets in the gradient image. The red dashed line at 5.96 $pA^2$ is the mean of the $I_{SC}$ variances within the identified facets. Based on the histogram, it is statistically unlikely that the mean of the current variances in the facets is random; the *p*-value is 0.02. See Supplementary Methods for details of gradient identification and mean variance calculation.

azimuthal gradient from the measured topography image (Fig. 3a), as shown in Fig. 3b. From the gradient image, the facets were individually identified on the basis of their constant gradient using segmentation and watershed algorithms (Supplementary Fig. 11). The variance of $I_{SC}$ values within each facet was calculated, and then averaged, yielding a mean of variances of 5.69 $pA^2$. Details of the variance calculation are available in the Supplementary Methods. To determine the significance of this mean value, the same calculation was performed on randomly selected areas of the $I_{SC}$ map that mimic the number and size of the identified facets. This process of randomly selecting areas was completed 2,000 times to generate the histogram of the mean of current variances shown in Fig. 3c, with

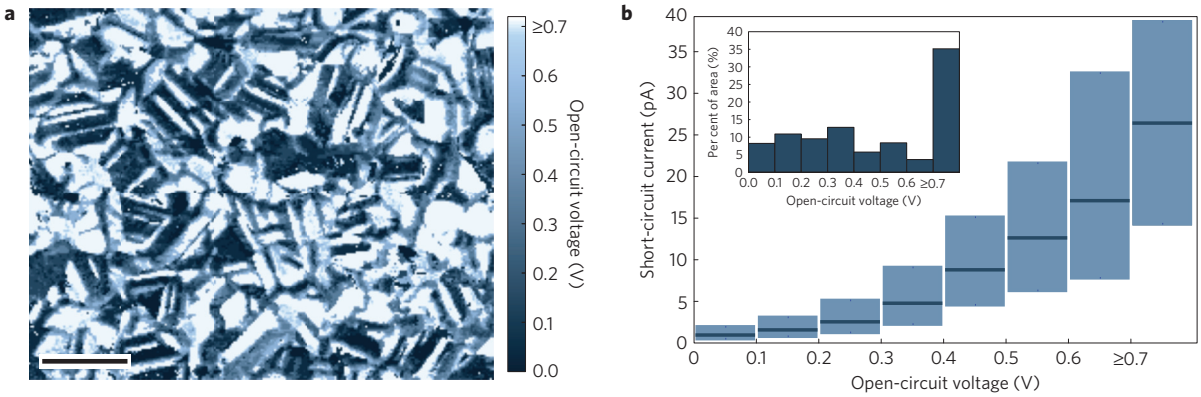


**Figure 4 | Heterogeneity in $V_{OC}$ and its correlation to $I_{SC}$. a**, Local $V_{OC}$ map generated by consecutively measuring photocurrent maps at reference biases from 0.1 to 0.7 V in increments of 0.1 V in the same area, and then aligning the images to assign $V_{OC}$ values to individual pixels. The scale bar is 500 nm. **b**, Box plot revealing the $I_{SC}$ range for each $V_{OC}$ interval in **a**. The top and bottom of each box indicate the first and third quartiles, respectively, and the dark horizontal lines indicate the median. Larger $V_{OC}$ correlates with higher $I_{SC}$. Inset: Area histogram of $V_{OC}$ intervals.

the majority of randomly placed areas exhibiting a mean variance of 7.5 $pA^2$. Since the current within the crystal facets has a mean variance significantly lower than the range of mean variance for randomly selected areas, the correlation of $I_{SC}$ heterogeneity with the crystal facets is statistically confirmed ($p$-value = 0.02). The same calculation was performed on another set of topography and $I_{SC}$ images for $MAPbI_{3-x}Cl_x$, and again the mean current variance for the facets was significantly less than for randomly selected areas (Supplementary Fig. 12). From this analysis, we conclude that the intra-grain variations in $I_{SC}$ and $V_{OC}$ are indeed facet dependent.

While the $I_{SC}$ heterogeneity on the length scale probed here might be partially compensated by long charge-carrier diffusion lengths, $V_{OC}$ inhomogeneity is the performance-determining factor for macroscale solar cells: $MAPbI_{3-x}Cl_x$ grains can be approximated as individual PV elements wired in parallel, where the lowest $V_{OC}$ will significantly reduce the macroscopic $V_{OC}$ (refs 19,30). If simply considering two adjacent grains, charges will flow from the high- to the low-$V_{OC}$ grain, reducing the overall $V_{OC}$. Hence, we investigated $V_{OC}$ variation in more detail by collecting consecutive photocurrent maps of the same area at forward reference biases from 0.1 to 0.7 V, with increments of 0.1 V, shown in Fig. 4a. These images were aligned, and the voltage values assigned based on two factors: if the photocurrent is approximately zero, $V_{OC}$ is set equal to the applied reference bias. If the current switches from positive ($V_{OC}$ higher than applied bias) to negative ($V_{OC}$ lower than applied bias) from one map to the next, $V_{OC}$ is between the two bias values. Values of $V_{OC}$ above 0.7 V are marked in white. Some areas are likely to have a higher $V_{OC}$ than 0.7 V, but we were not able to measure consecutive photocurrent maps for an applied bias range greater than 0.1 V to 0.7 V without tip modification. Any tip modification can change the tip–substrate contact area and tip work function, making quantitative current and voltage comparisons unreliable. We find a surprisingly large local variation in $V_{OC}$—over a range of 0.6 V—that has a dramatic impact on the macroscopic $V_{OC}$ and, hence, PCE. Again, the variation in $V_{OC}$ is correlated with the crystal facet that is being measured (Supplementary Fig. 13).

The spatial correlation between $V_{OC}$ and $I_{SC}$ indicated in Fig. 2 becomes more apparent when the full $V_{OC}$ range map in Fig. 4a is compared to the $I_{SC}$ map for that area (Supplementary Fig. 13), as illustrated in Fig. 4b. Higher $V_{OC}$ correlates with higher $I_{SC}$. Approximately 5% of the measured area was non-functioning with zero $I_{SC}$ and $V_{OC}$, while 35% of the area produced $V_{OC}$ greater than 0.7 V, suggesting that the efficiency in those areas is very high. If one were to assume a uniform fill factor, and gauge PCE only by the product of $V_{OC}$ and $I_{SC}$, high efficiency facets would perform up to 50% better than average, which would mean that some grains with specific facets could approach the theoretical PCE limit.

So far, we have not been able to specifically index the high- and low-efficiency facets: electron backscatter diffraction mapping gave no meaningful results on facet orientation due to damage from the electron beam. Furthermore, spatially resolved elemental analysis by energy dispersive X-ray spectroscopy and by scanning Auger microscopy (Supplementary Fig. 14) failed to find differences in chemical composition, with no detectable trace of chlorine across the surface, consistent with prior reports[31–33]. We considered a range of hypotheses to explain the observed heterogeneity, but most could not describe the experimentally observed facet dependence (see Supplementary Discussion). However, we note that recent findings from deQuilettes *et al.*[22] showed that inter-grain variation of PL intensity and lifetime are due to variations in trap state concentrations and that the traps can be passivated by surface treatment. Because PL efficiency is related to $V_{OC}$ (ref. 24), we hypothesize that our observed intra-grain heterogeneity in $V_{OC}$ is a consequence of variations in trap state concentrations among crystal facets: a high density of trap states lowers $V_{OC}$ due to Fermi level pinning and reduces $I_{SC}$ due to higher recombination rates. This hypothesis is further supported by Noel *et al.*[34] showing that surface passivation enhances $I_{SC}$, $V_{OC}$, and fill factor in PV devices equivalent in material and performance to those studied here. The simultaneous negative effect of trap states on $V_{OC}$ and $I_{SC}$ explains the strong spatial correlation we observe.

## Facet impact on internal electric fields and drift current

To confirm that the observed heterogeneity in $V_{OC}$ and $I_{SC}$ is not related to differences in mobility, we mapped the local drift current ($I_D$), which is proportional to mobility. We also note that $I_D$ is an important parameter for LED applications. The $I_D$ maps at 2 V and 3 V applied bias in Fig. 5a,b show that there is greater heterogeneity at 3 V compared to 2 V. An applied bias above 2 V provides sufficiently large electric fields across the perovskite film to ensure that current is dominated by electronic transport (Supplementary Fig. 15) rather than recombination at trap states[19,35,36]. The $I_D$ map at 2 V shows very little heterogeneity throughout individual grains and between grains, which indicates a relatively constant mobility at these length scales and bias conditions. This observation indicates that variations of mobility are not the cause of the $I_{SC}$ and $V_{OC}$ heterogeneity. However, at 3 V forward bias the heterogeneities become much more pronounced and reveal a reoccurrence of facet-dependent heterogeneity (Fig. 5b). To ensure reproducibility, we measured at 2 V, 3 V, and back to 2 V, showing no difference in the 2 V $I_D$ maps or topography (Supplementary Fig. 16).

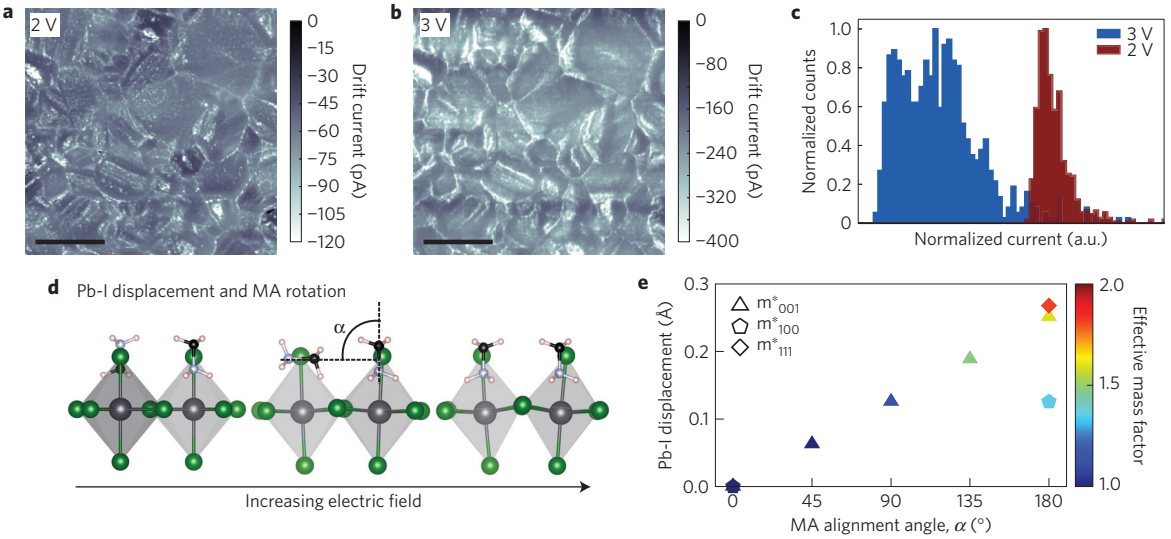


**Figure 5 | Heterogeneity in drift current due to changes in effective mass. a**, Dark drift current ($I_D$) map measured at a forward bias of 2 V indicates homogeneous electrical transport within grains. The scale bar is 500 nm. **b**, $I_D$ map measured at a forward bias of 3 V and in the same area reveals significant heterogeneity. The scale bar is 500 nm. **c**, Histogram of the relative drift currents at each pixel within a representative grain measured at 2 and 3 V, showing increased heterogeneity at 3 V. **d**, Application of sufficiently high electric fields results in alignment of the MA molecules along the electric field direction and a displacement of the Pb cations relative to $I_6$ octahedra. Grey, green, black, light blue, and white spheres represent Pb, I, C, N, and H atoms, respectively. The MA molecules are aligned in parallel at an alignment angle of $\alpha = 180°$. Enlarged images of these effects in Supplementary Fig. 20. **e**, The electron and hole effective masses increase as both the Pb ions are displaced and as the MA become more aligned with the electric field. The effective mass can increase by up to a factor of 1.8, depending on the electric field direction.

The enhancement of $I_D$ heterogeneity when moving from 2 to 3 V forward bias is illustrated in a histogram where the number of pixels is plotted versus the relative drift currents for an individual grain (Fig. 5c). The blue histogram represents $I_D$ at 3 V, the red histogram at 2 V. Due to the difference in $I_D$ magnitude measured at 2 and 3 V, the current values in the histograms are shifted and normalized to the respective mean currents and the histogram amplitudes are normalized to unity for easy comparison. The $I_D$ histogram at 3 V (blue) is very broad, with $I_D$ values ranging over an order of magnitude for different pixels. It shows two distinct peaks at −0.22 and −0.15 nA, which stem from two different facets within one grain, with one facet allowing 1.5 times higher $I_D$. In contrast, the 2 V histogram (red) is narrow and has only one peak at −65 pA, representing the spatial homogeneity of the measured mobility. Previously, ion migration was observed at comparable applied electric fields, which was indicated by modification of the topography[37]. However, due to our measurement technique, the sample is exposed to the maximum electric field for only 1.6 ms—too brief for ion migration[28]—when the tip is on the sample surface. The field is one order of magnitude lower during the next 10 ms, when the tip retracts, moves to the next pixel, and re-approaches. Based on the Einstein relation, which describes ion motion under an external force, and a diffusion coefficient of $10^{-12}$ cm$^2$ s$^{-1}$ (ref. 38), iodine ions will drift only 0.062 nm under a bias of 3 V across a 300 nm film over 1.6 ms. Hence, we would not expect topographic or $I_D$ modification for biases up to 3 V, consistent with our observations. We did not apply a bias over 3 V due to modifications in sample morphology at higher bias. While the $I_D$ homogeneity at 2 V supports the hypothesis that facet-dependent surface defect state concentrations give rise to local PV performance differences, the question remains: what causes the appearance of facet-dependent heterogeneity of $I_D$ at higher bias?

To address this question, we investigated the effect of large electric fields on the electronic structure of lead halide perovskites using first-principles DFT calculations including spin–orbit coupling (SOC). For electric fields larger than ~$10^5$ V cm$^{-1}$, corresponding to 3–4 V across our thin films, we find that the methylammonium (MA) ions align with the electric field (see Supplementary Methods). This alignment is accompanied by displacements of the Pb ions relative to the $I_6$ octahedra in each unit cell, leading to an overall polarization of the crystal lattice (Fig. 5d)[39–42]. As shown in Fig. 5e, this polarization results in an increase in the effective mass of electrons and holes along the direction of the electric field by a factor between 1.3 and 1.8 for the three directions of MA alignment examined. Assuming a constant charge density, $I_D$ is proportional to mobility and, thus, inversely proportional to the reduced effective mass, which increases under sufficiently large electric fields according to our DFT calculations.

The internal electric field in $MAPbI_{3-x}Cl_x$ films is approximately equal to $(V_{app} - V_{OC})/d$, where $V_{app}$ is the applied forward bias and $d$ is the film thickness. Hence, we suggest that at a bias of 3 V, only facets with low $V_{OC}$ (higher trap state density) have an internal electric field sufficiently high to induce complete MA alignment and the corresponding polar Pb and I displacements. The 1.3 to 1.8 times increase in effective mass, as predicted by our calculations, explains the experimentally observed reduction in $I_D$ of 1.5 times between different facets on the same grain. On facets characterized by high $V_{OC}$, the internal electric fields do not surpass the necessary threshold, and the mobility remains high. This model explains the facet-dependent heterogeneity in $I_D$ at large bias and its spatial correlation with $V_{OC}$ (Supplementary Fig. 17). We did consider other hypotheses to describe the heterogeneity at high bias, such as variations in carrier concentration, scattering time, and ion migration, but our model based on the DFT calculations provides the best agreement with the experimental results (see Supplementary Discussion). Ion migration may influence the measured magnitude of $I_D$, but its effect is probably very small (Supplementary Fig. 16). Facets with high trap state density can modify local $I_D$, an important insight for LED operation.

## Conclusion

In conclusion, we show significant intra-grain heterogeneity in short-circuit current, open-circuit voltage, and high bias drift current, as well as spatial correlation between these parameters, in

state-of-the-art $MAPbI_{3-x}Cl_x$ solar cell materials. The intra-grain heterogeneity in $V_{OC}$ and $I_{SC}$ is indicative of facet-dependent defect concentrations in these polycrystalline films. $V_{OC}$ heterogeneity has a direct effect on macroscale solar cell performance, but can also indirectly affect mobility due to local polarization at high forward bias, which might also impact LED applications. Based on these results, the efficiency of single-crystal and polycrystalline halide perovskite solar cells and LEDs can be systematically improved by controlling the growth direction of the grains and the orientation of the facets at interfaces with electron and hole conducting layers, as well as by chemical passivation of interfacial defect states. We are currently working toward growing high-quality $MAPbI_{3-x}Cl_x$ films with different preferential crystal orientations to measure changes in heterogeneity with cAFM for correlation with macroscopic PCE. Our findings described here suggest that reproducible performance of devices at the scale of individual grains will rely on control of facet-specific defect properties.

## Methods

**Conductive atomic force microscopy.** cAFM allows for the simultaneous measurement of current and topography. Measurements were performed using a Park Systems NX10 AFM encased in a nitrogen-filled glovebox to prevent sample degradation. Samples can be stored at least one week in the nitrogen atmosphere without degradation. All measurements were conducted with relative humidity less than 1%. The gentle PinPoint mode was the key to acquiring reproducible and reliable topography and cAFM images on the rough $MAPbI_{3-x}Cl_x$ surfaces: the tip approached over a period of 5 ms to achieve an interaction force of 2 nN, the force was held constant while the current was sampled 80 times at 50 kHz, then the tip retracted over a period of 5 ms (Fig. 1a) and moved to the next pixel. The height at constant force is also recorded to generate a simultaneous topographic image. This method differs significantly from tapping mode because a contact mode tip is used, the tip is not oscillating, and the tip retracts and approaches at each pixel rather than adjusting the tip height to maintain a constant oscillation amplitude. This scan mode does require more time (approximately 2 h for a 512 × 512 pixel image), but results in highly reproducible images. The drift on our Park NX10 microscope was typically 10 nm $h^{-1}$ in equilibrium (Supplementary Fig. 3), and successive current scans were digitally aligned using the topographic image channel; thus, drift did not complicate interpretation of the results presented here. We chose these approach–retract conditions to achieve reproducible photocurrent measurements and to avoid effects of ion migration[28] (see Supplementary Notes 2 and 3) since the tip is in contact for less than 1.6 ms with the sample—too fast for ion migration to play a role. In our cAFM set-up, the bias is applied to the fluorine-doped tin oxide (FTO) electrode, while the Pt tip is at virtual ground. The current is measured directly after the tip using a preamplifier with a gain of $10^{10}$ V/A. Because of this electrical configuration, negative voltage forward biases the cell and $I_{SC}$ has a positive value. Short-circuit current density ($J_{SC}$) values were not calculated for the nanoscale measurements, because determining the contact area between the AFM tip and the sample at each pixel would be a gross approximation. For the photocurrent maps, the sample is illuminated from above with a white LED having an output from 375 to 800 nm and an integrated power density of 2.73 mW $cm^{-2}$ (see Supplementary Fig. 18 for the spectrum). Since initial light exposure modifies the performance of lead halide perovskites, we light-soaked the samples for an hour before characterizing the local performance under steady state conditions. AdvancedTEC ContPt AFM probes (Nanosensors) were employed because the tetrahedral tip protrudes from the end of the cantilever, which provides direct optical access to the point of contact between the tip apex and the sample (see Supplementary Methods). Shading of the sample by the cantilever was also prevented by using a 0.4 numerical aperture objective, which focuses the light with a 24-degree half-angle. These tips have a 25 nm radius of curvature and a 0.2 N $m^{-1}$ force constant. Many tips were used to ensure that the tips were sharp and not contaminated by material from the perovskite surface. As soon as any tip modification was observed, we exchanged the tip. Data taken while the tip apex was modified were not considered for analysis.

**Sample preparation and device performance.** The two-step low-pressure vapour-assisted solution process to fabricate the $MAPbI_{3-x}Cl_x$ is described as follows[3]. First, a $PbI_2/PbCl_2$ solution is spin coated onto titanium dioxide ($TiO_2$) coated FTO glass substrates. Second, the film is converted to $MAPbI_{3-x}Cl_x$ by annealing the film in $CH_3NH_3I$ vapour at low pressure for 2 h. This fabrication technique creates continuous films and reduced hysteresis effects in a planar PV device architecture. Planar solar cells with the structure FTO/dense $TiO_2/MAPbI_{3-x}Cl_x$/2,20,7,70-tetrakis(N,N-di-p-methoxyphenylamine)–9,9-spirobifluorene (spiro-OMeTAD)/Au have an average PCE of 15.7%, $V_{OC}$ of 1.0 V, and short-circuit current density ($J_{SC}$) of 21.3 mA $cm^{-2}$ (ref. 3). A representative current density–voltage curve is shown in Supplementary Fig. 1. For the cAFM measurement, the $MAPbI_{3-x}Cl_x$ surface must be exposed to correlate morphology and current. To directly access the perovskite surface, the spiro-OMeTAD hole transport layer (HTL) and Au contact are omitted and the Pt-coated AFM tip acts as the electrode. A macroscale solar cell with a structure mimicking the cAFM measurement (FTO/$TiO_2$/$MAPbI_{3-x}Cl_x$/Pt) has a $V_{OC}$ of 0.51 V and $J_{SC}$ of 16.2 mA $cm^{-2}$ (see Supplementary Fig. 4 for a representative current–voltage curve). The significantly reduced $V_{OC}$ is the result of removing the $MAPbI_{3-x}Cl_x$/spiro-OMeTAD heterojunction, so only the $TiO_2/MAPbI_{3-x}Cl_x$ heterojunction contributes to the $V_{OC}$ (ref. 19).

**Python image analysis.** The Python code utilizes the Oriented FAST and Rotated BRIEF (ORB) binary descriptor to match objects in the images, and the RANSAC method is use to filter the matches to determine the transform[43]. Image registration allowed for careful comparisons of $I_D$, $I_{SC}$ and $V_{OC}$ of the exact same region. To compare $I_{SC}$ to the grain size, we used the watershed method to identify crystal grains and calculate the average $I_{SC}$ per grain.

**First-principles calculations.** To understand the consequences of internal electric fields on the atomic and electronic structure of $(CH_3NH_3)PbI_3$, we perform first-principles DFT calculations including spin–orbit coupling (SOC). DFT calculations were performed using the Perdew–Burke–Ernzerhof (PBE) exchange correlation functional[44] and the projector augmented wave (PAW)[45] formalism as implemented in the Vienna *ab initio* Simulation Program (VASP)[46]. The tetragonal phase is described by a $\sqrt{2} \times \sqrt{2} \times 2$ unit cell with four formula units, corresponding to a total of 48 atoms. We performed geometry optimizations of three structures with parallel alignment of the MA molecules in [001], [100] and [111] directions, using a 4 × 4 × 4 Γ-centred *k*-point mesh and an energy cutoff of 500 eV. Starting from experimental lattice parameters[3], we performed full structural relaxations where lattice constants, and internal degrees of freedom were allowed to relax. No symmetry constraints were imposed in these calculations, and forces were converged until smaller than 0.01 eV $Å^{-1}$. Band structures were calculated from charge densities obtained using a denser 6 × 6 × 6 Γ-centred *k*-point mesh, including semi-core states and spin–orbit interaction. Total energies and lattice parameters of all structures that we considered are shown in Supplementary Table 1. From the band structures, we calculated the effective electron and hole masses by parabolic band fitting around the conduction band minimum (CBM) and the valence band maximum (VBM), respectively, along the crystallographic high-symmetry directions. In the main text, we report the factor by which the reduced effective mass changes along the direction of MA alignment, since we assume that transport takes place along the direction of the applied electric field. For example, we show the factor by which the reduced effective mass changes along the crystallographic [001] direction on aligning the MA ions along this direction. This factor is defined as $m^{\alpha,*}{}_{001}/\ m^{\alpha=0^\circ,*}{}_{001}$, where $m^{\alpha,*}{}_{001} = m^{e}_{001} m^{h}_{001}/(m^{e}_{001} + m^{h}_{001})$ is the reduced effective mass for alignment angle $\alpha$, and $m^{e}_{001}$ and $m^{h}_{001}$ are the respective electron and hole effective masses along the crystallographic [001] direction. The effective masses of all structures that we considered can be found in Supplementary Table 2. See Supplementary Methods for more details of the DFT calculations.

Received 4 December 2015; accepted 26 May 2016; published 4 July 2016

## References

1. Burschka, J. *et al.* Sequential deposition as a route to high-performance perovskite-sensitized solar cells. *Nature* **499**, 316–319 (2013).
2. Eperon, G. E., Burlakov, V. M., Docampo, P., Goriely, A. & Snaith, H. J. Morphological control for high performance, solution-processed planar heterojunction perovskite solar cells. *Adv. Funct. Mater.* **24**, 151–157 (2014).
3. Li, Y. *et al.* Fabrication of planar heterojunction perovskite solar cells by controlled low-pressure vapor annealing. *J. Phys. Chem. Lett.* **6**, 493–499 (2015).
4. Noh, J. H., Im, S. H., Heo, J. H., Mandal, T. N. & Seok, S. I. Chemical management for colorful, efficient, and stable inorganic–organic hybrid nanostructured solar cells. *Nano Lett.* **13**, 1764–1769 (2013).
5. Tanaka, K. *et al.* Comparative study on the excitons in lead-halide-based perovskite-type crystals $CH_3NH_3PbBr_3$ $CH_3NH_3PbI_3$. *Solid State Commun.* **127**, 619–623 (2003).
6. Hao, F., Stoumpos, C. C., Chang, R. P. H. & Kanatzidis, M. G. Anomalous band gap behavior in mixed Sn and Pb perovskites enables broadening of absorption spectrum in solar cells. *J. Am. Chem. Soc.* **136**, 8094–8099 (2014).
7. Sum, T. C. & Mathews, N. Advancements in perovskite solar cells: photophysics behind the photovoltaics. *Energy Environ. Sci.* **7**, 2518–2534 (2014).
8. Tan, Z.-K. *et al.* Bright light-emitting diodes based on organometal halide perovskite. *Nature Nanotech.* **9**, 687–692 (2014).

9. Kazim, S., Nazeeruddin, M. K., Grätzel, M. & Ahmad, S. Perovskite as light harvester: a game changer in photovoltaics. *Angew. Chem. Int. Ed.* **53**, 2812–2824 (2014).
10. National Renewable Energy Laboratory *Best Research-Cell Efficiencies* www.nrel.gov/ncpv/images/efficiency_chart.jpg (accessed 17 May 2016).
11. Li, G. *et al.* Efficient light-emitting diodes based on nanocrystalline perovskite in a dielectric polymer matrix. *Nano Lett.* **15**, 2640–2644 (2015).
12. Xing, G. *et al.* Low-temperature solution-processed wavelength-tunable perovskites for lasing. *Nature Mater.* **13**, 476–480 (2014).
13. Hu, X. *et al.* High-performance flexible broadband photodetector based on organolead halide perovskite. *Adv. Funct. Mater.* **24**, 7373–7380 (2014).
14. Stranks, S. D. *et al.* Electron-hole diffusion lengths exceeding 1 micrometer in an organometal trihalide perovskite absorber. *Science* **342**, 341–344 (2013).
15. Xing, G. *et al.* Long-range balanced electron- and hole-transport lengths in organic-inorganic $CH_3NH_3PbI_3$. *Science* **342**, 344–347 (2013).
16. Dong, Q. *et al.* Electron-hole diffusion lengths >175 μm in solution grown $CH_3NH_3PbI_3$ single crystals. *Science* **347**, 967–970 (2015).
17. Wehrenfennig, C., Eperon, G. E., Johnston, M. B., Snaith, H. J. & Herz, L. M. High charge carrier mobilities and lifetimes in organolead trihalide perovskites. *Adv. Mater.* **26**, 1584–1589 (2014).
18. Oga, H., Saeki, A., Ogomi, Y., Hayase, S. & Seki, S. Improved understanding of the electronic and energetic landscapes of perovskite solar cells: high local charge carrier mobility, reduced recombination, and extremely shallow traps. *J. Am. Chem. Soc.* **136**, 13818–13825 (2014).
19. Edri, E. *et al.* Elucidating the charge carrier separation and working mechanism of $CH_3NH_3PbI_{3-x}Cl_x$ perovskite solar cells. *Nature Commun.* **5**, 3461 (2014).
20. Bergmann, V. W. *et al.* Real-space observation of unbalanced charge distribution inside a perovskite-sensitized solar cell. *Nature Commun.* **5**, 5001 (2014).
21. Yun, J. S. *et al.* Benefit of grain boundaries in organic–inorganic halide planar perovskite solar cells. *J. Phys. Chem. Lett.* **6**, 875–880 (2015).
22. deQuilettes, D. W. *et al.* Impact of microstructure on local carrier lifetime in perovskite solar cells. *Science* **348**, 683–686 (2015).
23. Bischak, C. G., Sanehira, E. M., Precht, J. T., Luther, J. M. & Ginsberg, N. S. Heterogeneous charge carrier dynamics in organic–inorganic hybrid materials: nanoscale lateral and depth-dependent variation of recombination rates in methylammonium lead halide perovskite thin films. *Nano Lett.* **15**, 4799–4807 (2015).
24. Tress, W. *et al.* Predicting the open-circuit voltage of $CH_3NH_3PbI_3$ perovskite solar cells using electroluminescence and photovoltaic quantum efficiency spectra: the role of radiative and non-radiative recombination. *Adv. Energy Mater.* **5**, 1400812 (2015).
25. Ballif, C., Moutinho, H. R. & Al-Jassim, M. M. Cross-sectional electrostatic force microscopy of thin-film solar cells. *J. Appl. Phys.* **89**, 1418–1424 (2001).
26. Visoly-Fisher, I., Cohen, S. R., Gartsman, K., Ruzin, A. & Cahen, D. Understanding the beneficial role of grain boundaries in polycrystalline solar cells from single-grain-boundary scanning probe microscopy. *Adv. Funct. Mater.* **16**, 649–660 (2006).
27. Groves, C., Reid, O. G. & Ginger, D. S. Heterogeneity in polymer solar cells: local morphology and performance in organic photovoltaics studied with scanning probe microscopy. *Acc. Chem. Res.* **43**, 612–620 (2010).
28. Chen, B. *et al.* Impact of capacitive effect and ion migration on the hysteretic behavior of perovskite solar cells. *J. Phys. Chem. Lett.* **6**, 4693–4700 (2015).
29. Nie, W. *et al.* High-efficiency solution-processed perovskite solar cells with millimeter-scale grains. *Science* **347**, 522–525 (2015).
30. Abass, A., Gestel, D. V., Wichelen, K. V., Maes, B. & Burgelman, M. On the diffusion length and grain size homogeneity requirements for efficient thin-film polycrystalline silicon solar cells. *J. Phys. Appl. Phys.* **46**, 45105 (2013).
31. Williams, S. T. *et al.* Role of chloride in the morphological evolution of organo-lead halide perovskite thin films. *ACS Nano* **8**, 10640–10654 (2014).
32. Tidhar, Y. *et al.* Crystallization of methyl ammonium lead halide perovskites: implications for photovoltaic applications. *J. Am. Chem. Soc.* **136**, 13249–13256 (2014).
33. Yu, H. *et al.* The role of chlorine in the formation process of '$CH_3NH_3PbI_3$-xClx' perovskite. *Adv. Funct. Mater.* **24**, 7102–7108 (2014).
34. Noel, N. K. *et al.* Enhanced photoluminescence and solar cell performance via Lewis base passivation of organic–inorganic lead halide perovskites. *ACS Nano* **8**, 9815–9821 (2014).
35. Guerrero, A., Juarez-Perez, E. J., Bisquert, J., Mora-Sero, I. & Garcia-Belmonte, G. Electrical field profile and doping in planar lead halide perovskite solar cells. *Appl. Phys. Lett.* **105**, 133902 (2014).
36. Ball, J. M., Lee, M. M., Hey, A. & Snaith, H. J. Low-temperature processed meso-superstructured to thin-film perovskite solar cells. *Energy Environ. Sci.* **6**, 1739–1743 (2013).
37. Yuan, Y. *et al.* Photovoltaic switching mechanism in lateral structure hybrid perovskite solar cells. *Adv. Energy Mater.* **5**, 1500615 (2015).
38. Eames, C. *et al.* Ionic transport in hybrid lead iodide perovskite solar cells. *Nature Commun.* **6**, 7497 (2015).
39. Leguy, A. M. A. *et al.* The dynamics of methylammonium ions in hybrid organic-inorganic perovskite solar cells. *Nature Commun.* **6**, 7124 (2015).
40. Li, J. & Haney, P. M. Molecular alignment and Rashba splitting in organometal halide perovskite $CH_3NH_3PbI_3$ absorbers. In *Photovoltaic Specialist Conference (PVSC), 2015 IEEE 42nd* http://dx.doi.org/10.1109/PVSC.2015.7355729 (2015).
41. Coll, M. *et al.* Polarization switching and light-enhanced piezoelectricity in lead halide perovskites. *J. Phys. Chem. Lett.* **6**, 1408–1413 (2015).
42. She, L., Liu, M. & Zhong, D. Atomic structures of $CH_3NH_3PbI_3$ (001) surfaces. *ACS Nano* **10**, 1126–1131 (2016).
43. van der Walt, S. *et al.* scikit-image: image processing in Python. *PeerJ* **2**, e453 (2014).
44. Perdew, J. P., Burke, K. & Ernzerhof, M. Generalized gradient approximation made simple. *Phys. Rev. Lett.* **77**, 3865–3868 (1996).
45. Blöchl, P. E. Projector augmented-wave method. *Phys. Rev. B* **50**, 17953–17979 (1994).
46. Kresse, G. & Furthmüller, J. Efficient iterative schemes for *ab initio* total-energy calculations using a plane-wave basis set. *Phys. Rev. B* **54**, 11169–11186 (1996).


## Acknowledgements

This material is based on work supported by the National Science Foundation Graduate Research Fellowship under Grant No. (NSF DGE 1106400) and by the Joint Center for Artificial Photosynthesis, a DOE Energy Innovation Hub, supported through the Office of Science of the US Department of Energy under Award Number DE-SC0004993. L.L. thanks the AvH foundation for financial support through the Feodor-Lynen program. D.Z. acknowledges support by the US Department of Energy, Office of Science, SBIR/STTR Program Office, under Award Number DE-SC0013212. A.W.-B., M.M., J.L. and S.Y.L. were supported by a DOE Early Career Grant. Work at the Molecular Foundry was supported by the US Department of Energy (DOE), Office of Basic Energy Sciences, Scientific User Facilities Division, under contract no. DE-AC02-05CH11231 and user proposal 4233. J.B.N., S.E.R.-L. and F.M.T. acknowledge support from the Laboratory Directed Research and Development Program at the Lawrence Berkeley National Laboratory under Contract No. DE-AC02-05CH11231.

## Author contributions

S.Y.L., L.L., F.M.T., I.D.S. and A.W.-B. conceived the work and designed the research strategy. S.Y.L. measured and analysed the cAFM data. E.W., M.M. and D.K.A. participated in and supported the development of the new cAFM technique. J.L., D.Z., P.D.A., D.F.O., S.W., F.M.T., I.D.S. and A.W.-B. participated in interpretation of the experimental data. L.L. and S.E.R.-L. performed the theoretical calculations supervised by J.B.N. Y.L. performed the sample preparation and macroscale characterization. I.D.S. and F.M.T. supervised the sample preparation and characterization. S.Y.L., L.L., D.F.O., I.D.S. and A.W.-B. wrote the manuscript with help from D.Z., P.D.A., and F.M.T. F.M.T., J.B.N., I.D.S. and A.W.-B. coordinated this research. All authors contributed to the scientific discussion and manuscript revisions.

## Additional information

Supplementary information is available online. Reprints and permissions information is available online at www.nature.com/reprints. Correspondence and requests for materials should be addressed to I.D.S. or A.W.-B.

## Competing interests

The authors declare no competing financial interests.